Engineering Structures 56 (2013) 779–793

Contents lists available at SciVerse ScienceDirect

Engineering Structures

journal homepage: www.elsevier.com/locate/engstruct

Modeling of microburst outflows using impinging jet and cooling source approaches and their comparison

Yan Zhang, Hui Hu, Partha P. Sarkar *

Department of Aerospace Engineering, Iowa State University, Ames, IA 50011, United States

ARTICLE INFO

Article history:
Received 17 December 2012
Revised 30 April 2013
Accepted 6 June 2013
Available online 9 July 2013

Keywords:
Microburst
Impinging-jet models
Cooling-source model
Laboratory simulation
PIV measurement
Numerical simulation
Field data comparison

ABSTRACT

Microbursts have been simulated and studied using different physical and numerical modeling methods. In the present study, the steady impinging jet model was comprehensively studied by using a 2-foot-diameter (0.61 m) microburst simulator available in the Department of Aerospace Engineering at Iowa State University. Point measurements and Particle Image Velocimetry (PIV) results revealed a detailed picture of the overall flow and distribution of velocity and turbulence in the outflow of the steady impinging jet. Comparisons suggested that the average wind velocity profile of the steady impinging jet matched well with those derived from field data and previous research. FFT of the velocity time-history and instantaneous PIV results implied that the outflow consisted of low-frequency periodic shedding of vortices and the steady impinging jet model could be seen as an ensemble average of a series of simulated microburst events. Due to lack of time-dependent evolutionary information of the steady impinging jet model, a transient impinging jet model was studied to capture the transient features which were then compared with those of the cooling-source model by performing numerical simulations. Transient features of the transient impinging jet model and cooling source model showed several differences mainly related to the different formation and transportation process of the primary vortex. Ground surface pressure distributions were found to be different due to different forcing parameter of the two models. Comparison with the field data suggested that both models resembled the dynamic features of a real microburst outflow. However, results showed that the cooling source model could produce a reasonable instantaneous radial velocity profile at maximum wind condition, while the transient impinging jet model resulted in a large deviation. Finally, merits and demerits of each modeling methods were discussed.

1. Introduction

A microburst is defined as an intense downdraft impacting the ground and forming a damaging outflow with a diameter less than 4 km [1]. Since 1970s, a number of field projects had been conducted to study this natural phenomenon, mainly within the meteorological society [2–5]. Microbursts are dramatically different from the traditional straight-line winds and other wind hazards. They could produce significant wind shear and extreme winds near ground with a wind profile differing from the atmospheric boundary layer. Due to its transient nature, microbursts usually have very short lifespan and large vertical velocity components, which make it difficult to be detected and studied by Doppler radar. Therefore, different engineering models have been developed and used to produce microburst-like flow fields for a variety of research purposes.

Microburst-modeling methods to date can be classified into three categories, i.e. ring-vortex modeling, impinging jet modeling, and cooling source modeling. The first method has mainly focused on revealing the structure and evolution of flow patterns around the primary vortex generated in a microburst. Ivan [6] described a mathematical model of a downburst that resolves the stream function around a ring vortex. It was reported that this model produced results resembling some of the flow patterns, particularly the primary-vortex pattern noted in field data from the JAWS project. Schultz [7] constructed a multiple vortex-ring model by using time-invariant vortex ring filaments from potential flow theory. The velocity distribution around this simulated ring vortex matched the field data of the 1985 DFW microburst reasonably well. Vicroy [8] compared three theoretical models: linear, vortex-ring, and empirical. He found that latter two types provided more favorable results than the linear model.

The impinging jet model has been widely adopted due to its simplicity and ability to produce reasonable outflow-velocity profiles. As early as in 1987, by summarizing field data collected from a series of Colorado microbursts during the JAWS project, Hjelmfelt [4] pointed out that the outflow structures were found to have features resembling those of a laboratory-simulated wall jet. Subsequently, the impinging-jet model was utilized, both numerically

* Corresponding author. Tel.: +1 5152940719.
E-mail address: ppsarkar@iastate.edu (P.P. Sarkar).

0141-0296/$ - see front matter © 2013 Elsevier Ltd. All rights reserved.
http://dx.doi.org/10.1016/j.engstruct.2013.06.003

and experimentally, by a number of researchers for microburst studies. Selvam and Holmes [9] used a two-dimensional k–ε model to simulate impingement of a steady jet of air on a ground plane. A reasonable agreement between numerical results and field data was achieved. Holmes [10] and Letchford and Illidge [11] performed experimental studies using a jet impinging on a wall to investigate topographic effects of a microburst outflow on velocity profiles. Holmes and Oliver [12] empirically combined wall-jet velocity and translational velocity and obtained a good representation of a travelling microburst which was well correlated with a 1983 Andrews AFB microburst. Wood et al. [13] experimentally and numerically studied impinging jets over various terrains. This study found agreement with respect to the established steady outflow at distances beyond 1.5 jet diameters from the impingement center. Choi [14] carried out both field and laboratory studies on a series of Singapore thunderstorms. Terrain sensitivity of microburst outflows was studied by comparing microburst observations at different heights and impinging jet experiments with different H/D ratios. The study produced similar trends, reflecting the impinging jet model's good capability for dealing with such problems. Chay et al. [15] conducted steady simulation and obtained good agreement with downburst wind-tunnel results. A non-turbulent analytical model was also used to study velocity–time history at a single point. Kim and Hangan [16] and Das et al. [17] performed both steady and transient two-dimensional CFD studies using an impinging jet model, producing reasonable radial–velocity profiles and good primary-vortex representation. Sengupta and Sarkar [18] carried out laboratory and 3-D numerical simulations using an impinging jet model. Both numerical and PIV results showed good agreements with full-scale data. To physically capture transient features, Mason et al. [19] deployed a pulsed-jet model to simulate transient microburst phenomenon. The formation and evolution of the primary, successive intermediate, and trailing edge vortices were visualized and recorded. Additionally, Nicholls et al. [20], Chay and Letchford [21], Letchford and Chay [22], and Sengupta et al. [23] performed impinging jet simulations to study the effects of microburst winds on low-rise structures. Generally, the impinging jet model is driven by a momentum-forcing source without any buoyancy effects. Although the steady-state models of impinging jet flow has been validated with field data by comparing wind velocity profiles, the transient features of an impinging jet flow compared to those of a real microburst still remain unknown.

An alternative approach using thermal cooling source was adopted by a few researchers, which puts more emphasis on the negative buoyancy and the dynamic development of the microburst. Experimentally, this method was accomplished by dropping denser fluids into less dense surroundings, which can be found in Lundgren et al. [24], Yao and Lundgren [25], and Alahyari and Longmire [26]. Nevertheless, the scale of physical modeling has remained very limited, making it almost impossible to study the wind loading effects on reasonably-scaled building models. Numerical simulations using cooling source approach involves a cooling source function, which was suggested by Anderson et al. [27]. The atmospheric full-cloud model was simplified to a space- and time-dependent cooling source function without considering the micro-physical process of a real microburst. This model was later used by Orf et al. [28] to study colliding microbursts, and by Orf and Anderson [29] to study travelling microbursts. Mason et al. [30] also investigated topographic effects on simulated downbursts using a sub-cloud model. Comparing the simulation results to their previous impinging jet modeling results, they suggested that little discrepancy was found with respect to the topographic effects despite use of two different modeling methods. Most recently, Vermeire et al. [31] compared the non-dimensional results using cooling source model and transient impinging jet model, and claimed that the impinging jet results deviated significantly from the cooling source results due to its unrealistic forcing parameters. This study used simplified impinging jet and cooling-source models and did not compare the simulation results with the transient characteristics of the field data. More comparisons with field data and data obtained from laboratory and numerical simulations are needed to compare and validate these two models apart from improving the models themselves.

Overall, due to the scarcity of field data and the complexity of this natural phenomenon, it is of critical importance to know which modeling method is the best for microburst study, particularly from an engineering point of view. Despite significant efforts by previous researchers, very little research has been found that compares the merits and demerits of different microburst models. In the present study, a steady impinging jet model was investigated by taking point and PIV measurements. Although the time-averaged characteristics of a microburst have been studied previously, its transient behavior and hence its dynamic features have not been fully explored. To complement the experimental study of a steady-impinging jet model, the transient behavior of an impinging jet model was studied numerically and compared with a simplified cooling source model. All results were compared to field data collected in the NIMROD and JAWS projects. Finally, the merits and demerits of these modeling methods were analyzed and concluded to provide references for use in future studies.

2. Experimental setup

The microburst was physically generated by a steady impinging jet flow simulator in the WiST (Wind Simulation and Testing) Laboratory at Iowa State University, shown in Fig. 1. The jet flow is produced constantly by a fan on the top and impinges on a wooden plate to form a steady wall-jet flow field. The diameter of the nozzle is about 0.6 m (2 feet). The distance between the nozzle exit and the plate representing the ground plane is adjustable from 1 to about 2.3 times the diameter (D) of the nozzle (0.75–7.5D in nature). The fan on the top of the simulator is driven by a step motor (RELIANCE ELECTRIC Duty-Master, Model number P2167403L). A honeycomb and several screens are placed at the exit of the nozzle to produce a uniform velocity across the exit and reduce the turbulence of the issuing jet. The axial velocity of the jet was measured at one nozzle diameter underneath the nozzle exit at different fan speeds, and the distribution across the jet was found to be sufficiently uniform, as shown in Fig. 2. The mean jet velocity under the nozzle exit was $V_{jet} \approx 6.9$ m/s.

Velocity measurements were first performed at different r/D locations (i.e. $r/D = 1$, 1.5, 2, 2.5) using three-component cobra-probe (TFI Pvt. Ltd.), where r is the radial distance from the center. Using this multi-hole probe, three components and the overall magnitude of the velocity vector can be measured at the same time. At each r/D location, measurements were taken at 38 points ranging from 0.25 in. to 7 in. above the ground plane. For each point, the data was collected at a frequency of 1250 Hz for 10 s. The measurement error was within ±0.5 m/s according to the specified accuracy of the cobra-probe. However, the probe could only resolve velocity information for the incoming flow within ±45° of the probe's axis. Therefore, for the shear layer of the wall jet flow, which is dominated by large-scale vortex structures, the accuracy of statistical results within the shear layers is significantly reduced due to reduced quantity of valid data gathered by the probe. PIV (Particle Image Velocimetry) technique was used (schematic is shown in Fig. 3) to capture whole-field information of the near-ground wall jet flow. The coordinate system indicating three velocity components was also shown in Fig. 3. The flow was seeded with 1–5 μm oil droplets and illumination was provided by a

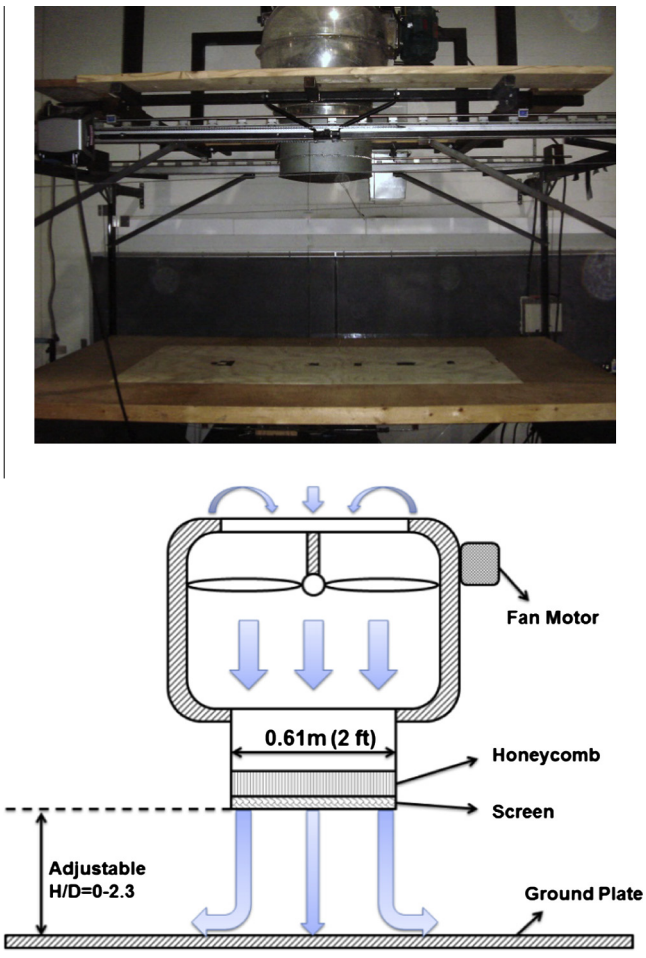

Fig. 1. Microburst simulator in WiST Lab at Iowa State University.

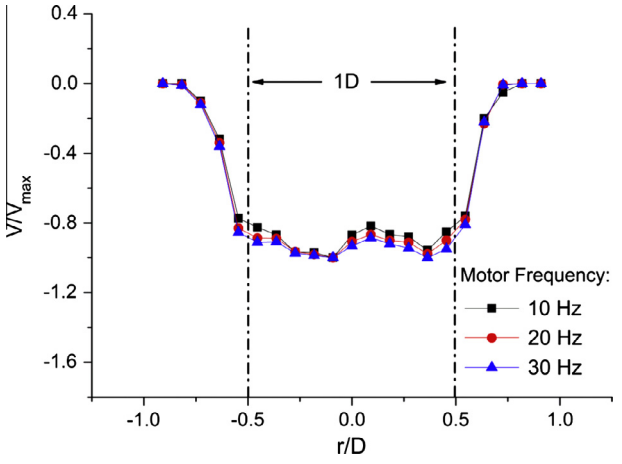

Fig. 2. Axial-velocity distribution across the jet (Experiment, Cobra-probe).

double-pulsed Nd:YAG laser (NewWave Gemini 200) adjusted on the second harmonic frequency and emitting two 200 mJ laser pulses at a wavelength of 532 nm and with a repetition rate of 10 Hz. The laser beam was shaped into a laser sheet (thickness ~1 mm) by using a set of mirrors along with spherical and cylindrical lenses. A high-resolution (1365 × 1024 pixels) charge-coupled device (CCD) camera with axis perpendicular to the laser sheet was used for PIV image acquisition. The CCD camera and the double-pulsed Nd:YAG lasers were connected to a workstation via a

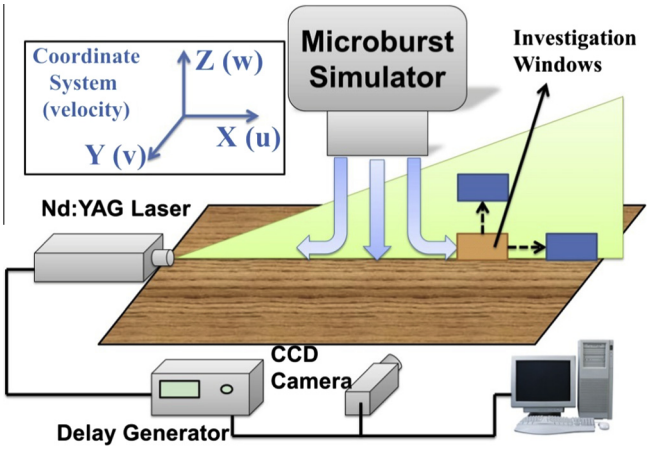

Fig. 3. Schematic of the PIV system.

digital delay generator that controlled the timing of both the laser illumination and the image acquisition.

The CCD camera was focused on a measurement window of 207 × 152 mm size such that a total of 14 windows were used to cover the entire microburst outflow region's areas of interest. The layout of these investigation windows is illustrated in Fig. 4. To ensure that results from different windows match each other reasonably well, 30% overlaps were established between each window and its vertically-adjacent window. Instantaneous PIV velocity vectors were obtained using a frame-to-frame cross-correlation technique involving successive frames of patterns of particle images in an interrogation window with 32 × 32 pixels and an effective overlap of 50% to satisfy the Nyquist criterion. After the instantaneous velocity vectors were determined, time-averaged quantities such as mean velocity, turbulent-velocity fluctuations, normalized turbulent kinetic energy, and Reynolds stress distributions were obtained from a cinema sequence of 500 frames of instantaneous velocity fields for each case. The measurement uncertainty level for the velocity vectors was estimated to be within 2.0%, and that of the turbulent velocity fluctuations and turbulent kinetics energy was about 5.0%.

3. Numerical simulation

3.1. Computational parameters

An axisymmetric unsteady RANS (Reynolds Averaged Navier–Stokes) model was used in this study using commercially available software FLUENT 12.1 (ANSYS Inc.). Although LES has the well-known ability to resolve large-scale turbulent structures and simulate time-dependent turbulent flows, the application of LES

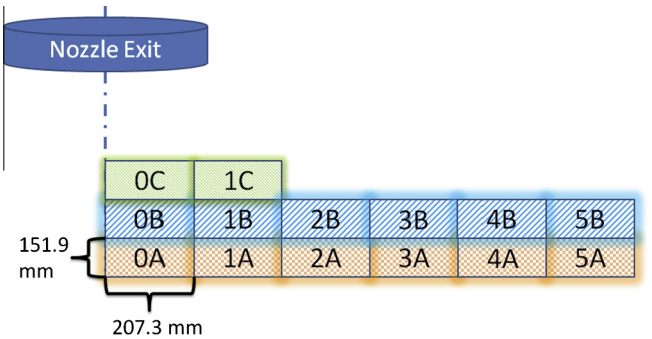

Fig. 4. Layout of investigation windows for PIV measurements.

requires a very fine mesh and sufficiently small time steps. Given the large geometric scale of the computational domain, use of LES could be extremely expensive for this problem with relatively high-Reynolds-number. The objective of this numerical simulation, however, was to investigate the differences of macro-scale flow features between two modeling methods and compare these features with the field data. Therefore, unsteady RANS or URANS model was used because it is proved to be economic and effective for this study. In the URANS simulation, the ensemble-averaged velocities, denoted by $\langle u \rangle$, are still functions of time, so the Reynolds decomposition of velocity can be expressed as $u = \langle u \rangle + u' = \bar{u} + u'' + u'$, where $\bar{u}$ is the time-averaged velocity, u'' is the resolved unsteadiness of the mean flow and u' is the fluctuating component of velocity. Therefore, the unsteady features of the ensemble-averaged flow field are resolved, making URANS an effective tool for solving only macro-flow problems.

The governing equations for the numerical simulation in Cartesian coordinate system are given as follows:

Continuity

$$\frac{\partial \rho}{\partial t} + \frac{\partial}{\partial x_i}(\rho u_i) = 0 \tag{1}$$

Momentum

$$\frac{\partial}{\partial t}(\rho u_i) + \frac{\partial}{\partial x_j}(\rho u_i u_j) = -\frac{\partial p}{\partial t} + \frac{\partial}{\partial x_j}\left[\mu\left(\frac{\partial u_i}{\partial x_j} + \frac{\partial u_j}{\partial x_i} - \frac{2}{3}\delta_{ij}\frac{\partial u_k}{\partial x_k}\right)\right] + \frac{\partial}{\partial x_j}\left(-\rho\overline{u_i' u_j'}\right) + f_i \tag{2}$$

The Reynolds stress term $-\rho\overline{u_i' u_j'}$ needs to be modeled to close the equation. Generally, the Reynolds stress term was modeled based on Boussinesq hypothesis as $-\overline{u_i' u_j'} = 2\nu_t S_{ij} - \frac{2}{3}k\delta_{ij}$, where $S_{ij} = \frac{1}{2}\left(\frac{\partial u_i}{\partial x_j} + \frac{\partial u_j}{\partial x_i}\right)$ and ν_t is newly introduced turbulence eddy viscosity term. f_i is the gravitational force term, which was considered in the cooling source model but set to zero in the impinging jet model.

For the cooling source model, the energy equation was also included

$$\frac{\partial}{\partial t}(\rho E) + \frac{\partial}{\partial x_i}(u_i(\rho E + p)) = \frac{\partial}{\partial x_i}\left(K_{eff}\frac{\partial T}{\partial x_i}\right) + Q_s \tag{3}$$

where $Q_s = Cp \cdot Q(x, y, t)$ is a source term which will be discussed later (Cp is the specific heat of air).

In the present study, the standard k–ε model was used to solve the turbulence eddy viscosity term. Such models are widely used due to their simplicity, robustness, and reasonable accuracy over a wide range of turbulent flows. The turbulence eddy viscosity was defined as $\nu_t = \frac{\mu_t}{\rho} = C_\mu \frac{k^2}{\varepsilon}$, where k is turbulence kinetic energy and ε is its rate of dissipation. Transport equations for k and ε could be found in Launder and Spalding [32] and the default model parameters were set in FLUENT during the simulation ($C_{1\varepsilon} = 1.44$, $C_{2\varepsilon} = 1.92$, $C_\mu = 0.09$, $\sigma_k = 1.0$, $\sigma_\varepsilon = 1.3$). A second order upwind scheme was used for solving the continuity and momentum equations and T.K.E. and turbulent dissipation rate were both determined using the Quadratic Upstream Interpolation for Convective Kinematics (QUICK) scheme. The SIMPLE scheme was used to provide pressure–velocity coupling. For the transient formulation, a second-order implicit scheme was adopted.

Both impinging jet and cooling source models were solved on a 2D axisymmetric domain. As shown in Fig. 5a, only w velocity in z direction and u velocity in r direction were considered in this simulation and swirling velocity was zero. To simulate the realistic microburst phenomena while keeping the computational domain in consideration, the jet diameter (D) and the jet-nozzle height from ground plane (H) were each set as 2500 m such that the H/D ratio was 1. These figures were well within the range of diameter D and H/D for a microburst, known to be varying between 400–4000 m and 0.75–7.5, respectively. For the steady impinging jet, a velocity inlet combined with an incompressible flow condition was used. For the cooling source model, a specific cooling function covering the inlet region was incorporated by adding a source term into the energy function. This cooling function will be discussed in detail later. A pressure inlet and compressible flow condition were used to resolve a density change induced by the cooling function.

All simulations in this study were solved on a structured grid with quadrilateral cells. At the wall boundary, the distance

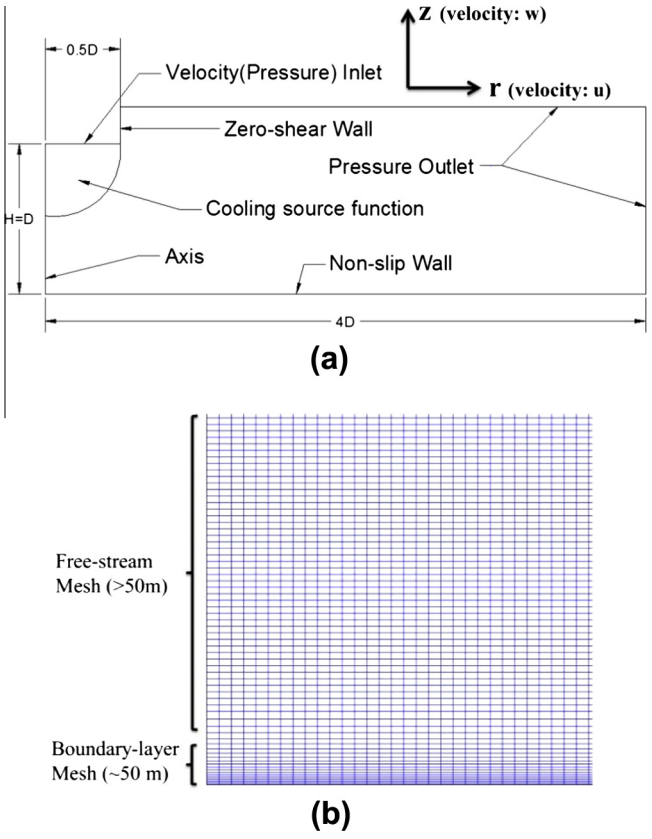

Fig. 5. (a) Computational domain, and (b) typical grid structure near wall boundary.

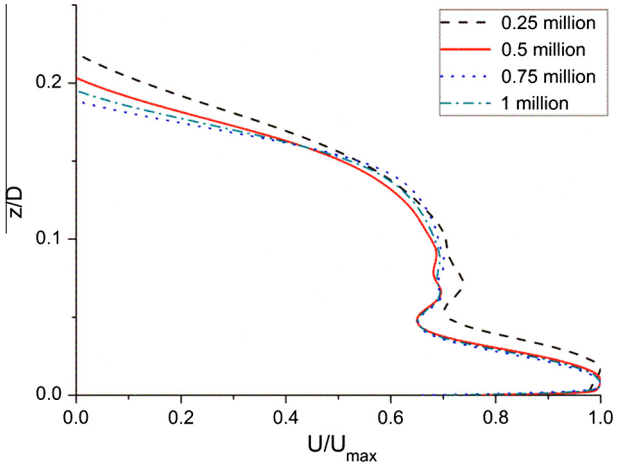

Fig. 6. Study of mesh independence (Normalized velocity at $r/D = 1.0$).

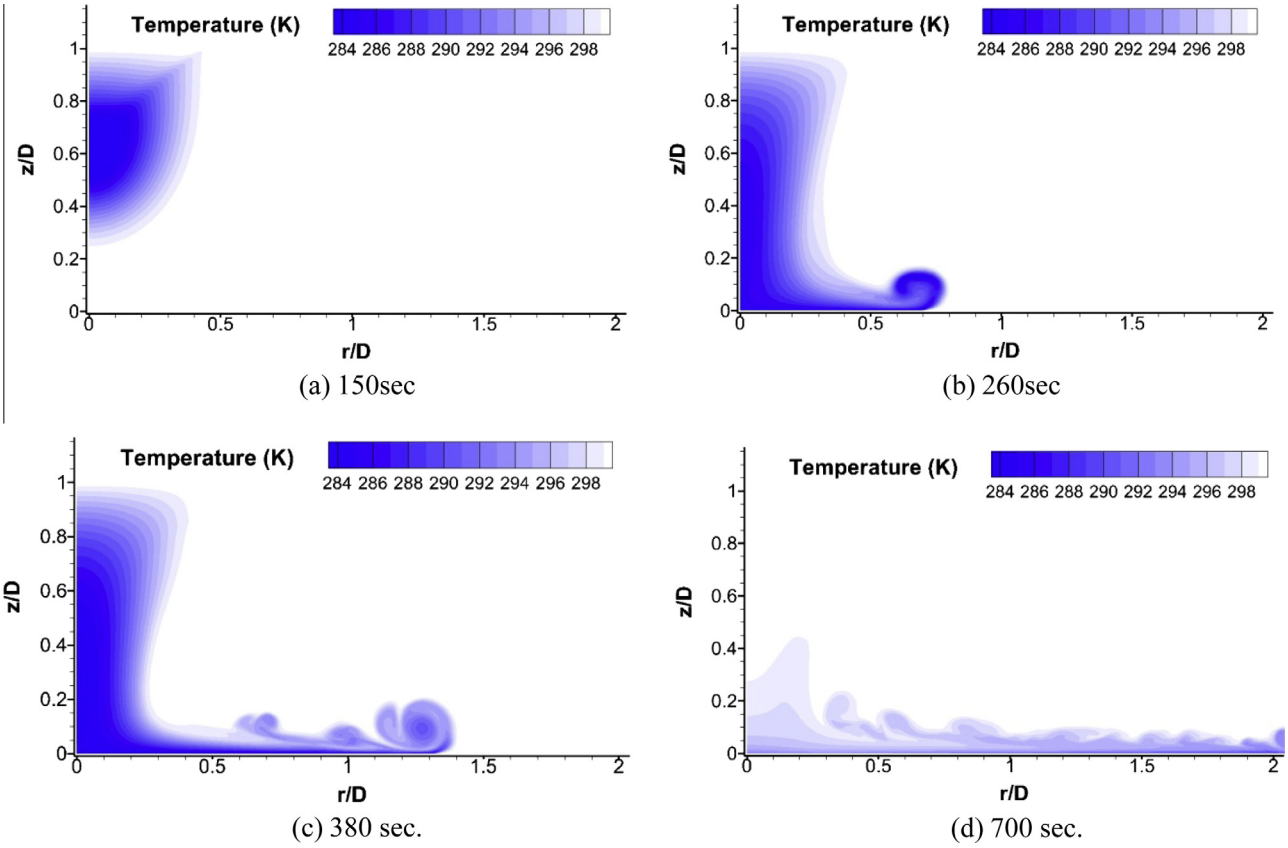

Fig. 7. Evolution of the temperature field in cooling source model (Numerical simulation).

Table 1
Scaling parameters for the numerical analysis.

	V_0	T_0	L_0	Re
Impinging jet	V_{01} = 45.9 m/s	T_{01} = 470 s	$L_{01} = 2.16 \times 10^4$ m	6.55×10^{10}
Cooling source	V_{02} = 67.5 m/s	T_{02} = 260 s	$L_{02} = 1.76 \times 10^4$ m	7.84×10^{10}

between the first row of grids and the ground was confined to be less than 1 m. The mesh was gradually stretched as it moved away from the ground-plane boundary and the cell spacing became constant above approximately 50 m from the ground level, as shown in Fig. 5b. A study of mesh independent was carried out separately before settling on the mesh. As shown in Fig. 6, all the radial velocity profiles for the impinging-jet model (at the $r/D = 1$ location at the 470 s time step) tend to converge to the same line as the number of cells increases. Therefore, a 1-million-cell grid was chosen and it should be safe to believe that the results are independent of mesh conditions.

3.2. Cooling function

A cooling source model was simulated by adding a spatial and temporal cooling source to the computational domain, as shown in Fig. 5. This sub-cloud cooling model was suggested by Anderson et al. [27]. This effect is achieved by adding a spatio-temporal source term to the energy equation described by:

$$Q(x,y,t) = \begin{cases} g(t)\cos^2 \pi R & \text{for } R < \frac{1}{2} \\ 0 & \text{for } R > \frac{1}{2} \end{cases} \quad R^2 = \left(\frac{x - x_0}{h_x}\right)^2 + \left(\frac{y - y_0}{h_y}\right)^2$$

where $g(t) = A\sin^2(\pi t/2\tau)$ K/s is a time-dependent coefficient which ramps up from 0 to a maximum ($A = -0.1$ K/s) in the first 120 s and then $g(t) = A\sin^2(\pi(540 - t)/2\tau)$ gradually decreases to 0 in the interval from 420 s to 540 s. τ is a time constant which was set to be 120 s in the present study. Between 120 s and 420 s, $g(t)$ was kept constant at a maximum intensity of $g(t) = A$, which is larger than that described in Anderson et al. [27] to obtain more significant cooling effects. R is non-dimensional radius (0–1) of the cooling source (elliptical in shape) determined by position of the geometric center (x_0, y_0) of the ellipse (x, y) and the major and minor half axes of the ellipse, h_x and h_y. Mason et al. [33] pointed out that changing the temporal term of the cooling function almost did not affect the normalized velocity profiles, while the geometric shape of the cooling source have a great influence on the results. However, the choice of the current simplified cooling function was made by Anderson et al. [27] based on a comparison of the numerical full cloud model and the real field events, and it was further utilized by Orf et al. [28] based on the micro-physical calculations for a downburst producing storm and by Vermeire et al. [31] for a model comparison. Therefore, the cooling function used here, though simplified, could be seen as a reasonable approximation. Fig. 7 illustrates the entire life-cycle of a simulated microburst event visualized by the evolution of the temperature field of the cooling source model.

3.3. Scaling parameters

To compare the transient features of the two numerical models, the flow-field variables of the models should be normalized to common critical parameters. Since the forcing mechanism is intrinsically different between the impinging jet model and the

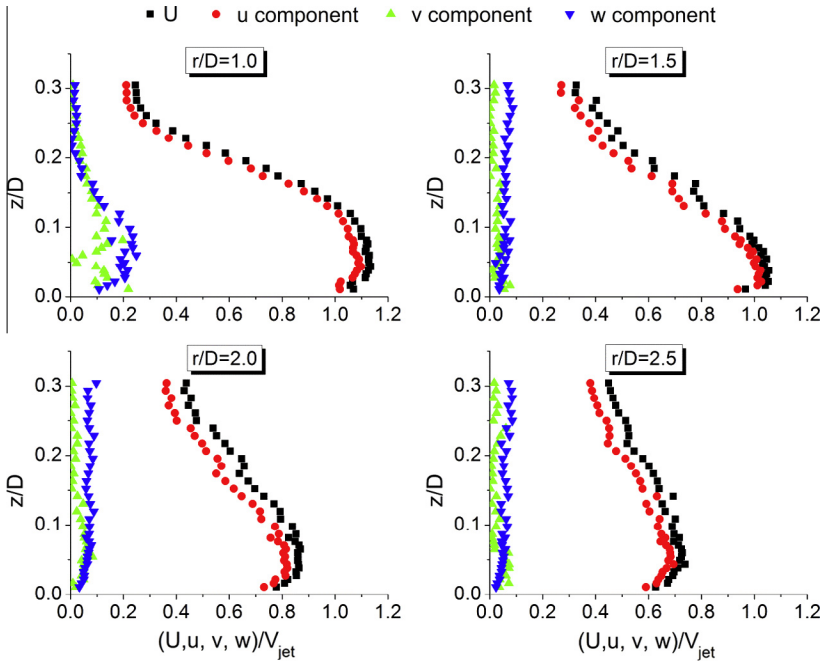

Fig. 8. Normalized componential radial–velocity profiles for H/D = 1 case (Experiment, Cobra-probe).

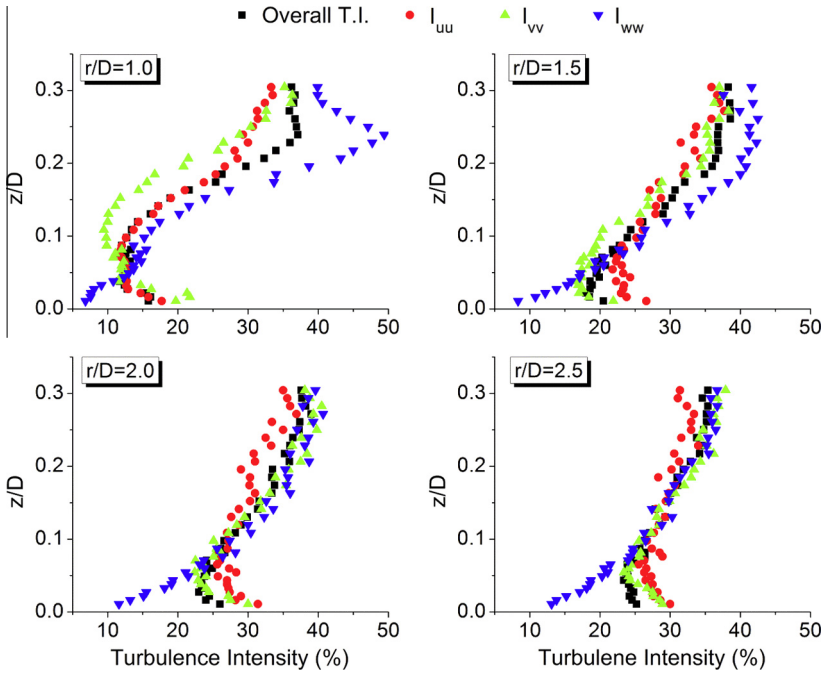

Fig. 9. Componential turbulence intensity component profiles for H/D = 1 case (Experiment, Cobra-probe).

cooling source model, it was decided not to directly match the results based on the computational time and length scales.

As is widely known, the most prominent feature of a microburst is the primary vortex ring that is known to produce extreme wind velocity. Therefore, the time scale T_0 was taken here as the computational time in each of the two modeling results at which maximum radial velocity (V_0) occurred. The velocity parameter was taken as V_0 and the length scale was calculated as $L_0 = V_0 T_0$. The corresponding Reynolds number would be

$$Re = \frac{V_0 L_0}{v}$$

Numerical scaling parameters for this case study are given in Table 1. It can be seen that the Reynolds numbers with the characteristic length L_0 are of the same order if using this scaling method.

4. Results and discussions

4.1. The steady impinging jet model

4.1.1. Overall/componential velocity and turbulence intensity profiles

A well-developed steady impinging jet flow normally consists of three flow regions: downdraft region, stagnation region and

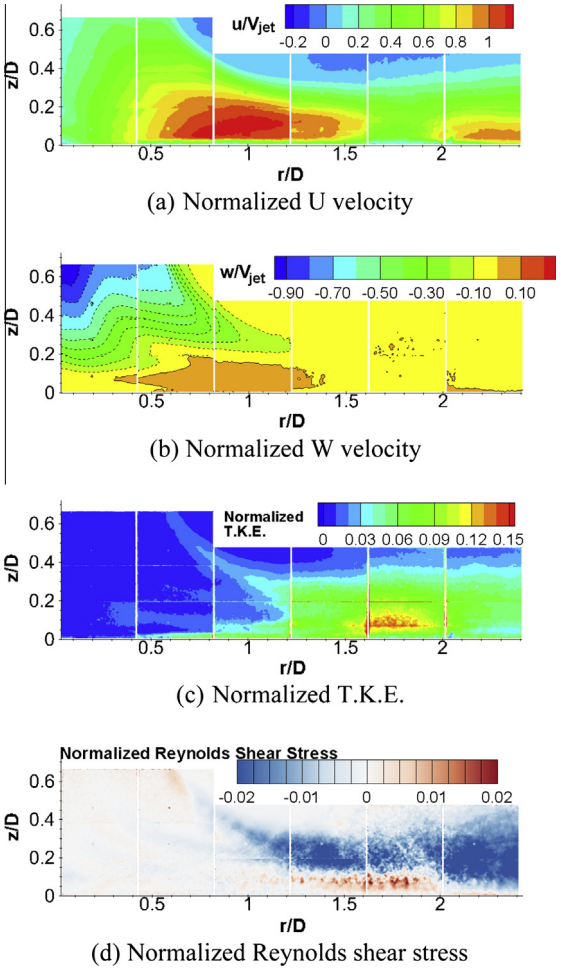

Fig. 10. Ensemble-averaged flow fields for $H/D = 1$ case (Experiment, PIV).

the wall jet region. The flow field of the wall jet region is usually more complex than the other two flow regions and of greater importance for engineering. Fig. 8 shows the total velocity (U) and velocity components (u, v, w) normalized by mean jet velocity (V_{jet}) at different radial locations $r/D = 1$, 1.5, 2, and 2.5 for H/D = 1 case, where r/D is the radial distance from the center normalized by the jet diameter. The vertical distance from the ground (z) was normalized by the jet diameter (D). Here, u denotes the mean velocity in the radial direction, while v and w denote the mean

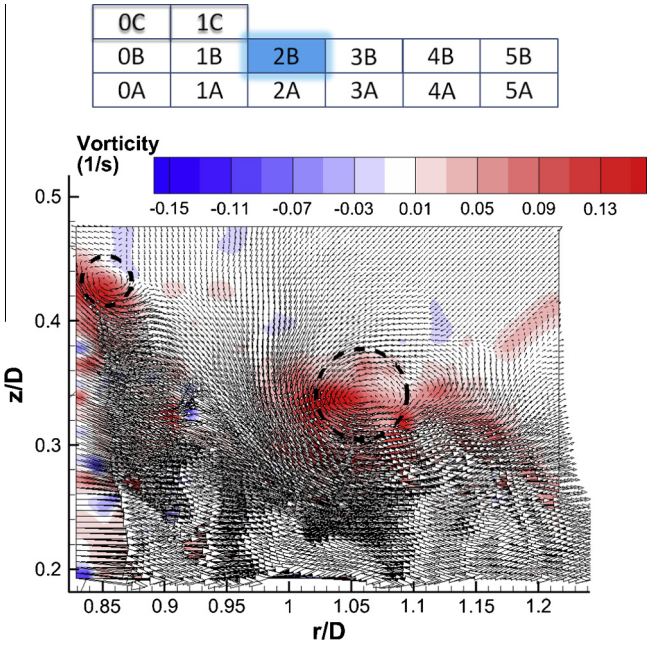

Fig. 12. A snapshot of the instantaneous vorticity field (Experiment, PIV).

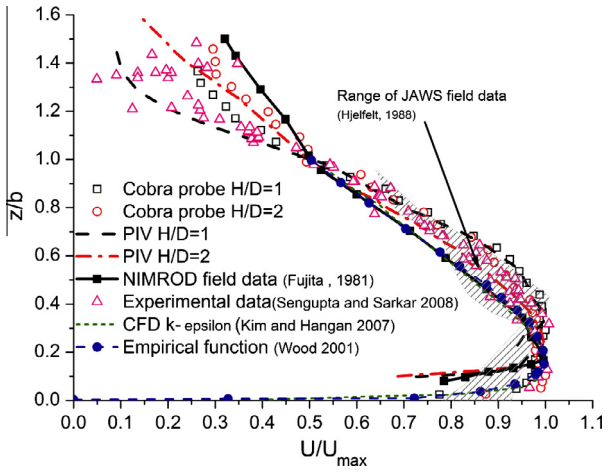

Fig. 13. Comparison of velocity profiles at the maximum velocity location ($r/D = 1$) (Experiment).

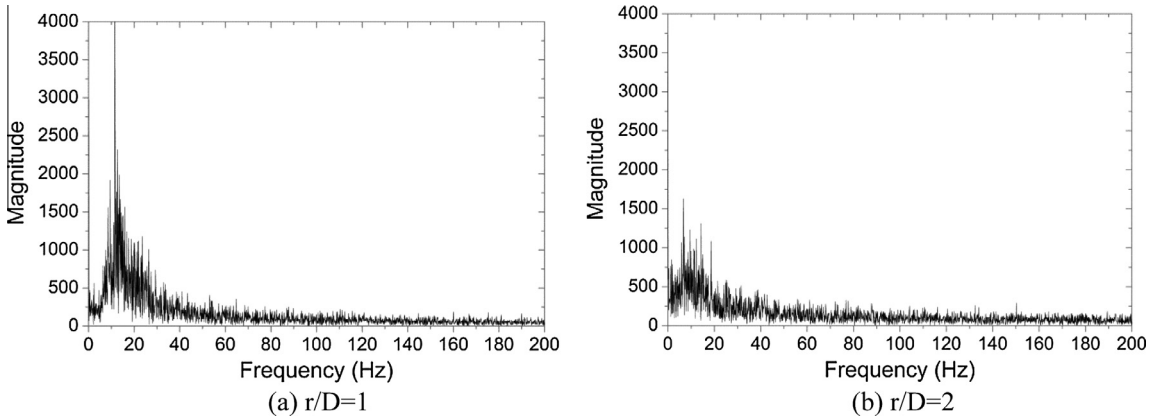

Fig. 11. Frequency spectrum of the radial–velocity fluctuation at $z/D = 0.20$ (Experiment, Cobra-probe).

velocity in tangential and axial directions respectively, of the impinging-jet flow.

Generally, the overall velocity distribution in vertical direction shows a wall-jet shape Maximum velocity was found at a height around $z/D = 0.05$ (corresponding to 20–200 m above ground level in a real microburst event). As radial locations moved from $r/D = 1$ to 2.5, maximum velocity decreased and the slope of velocity with elevation also reduced significantly. The radial velocity (u) was found to be dominant for all radial locations. However, it is interesting to observe that a considerable increase of the magnitudes of v and w component occurred at $r/D = 1$ from the ground to $z/D = 0.1$. This phenomenon was possibly related to the channeling effect between the primary vortex and the secondary vortex, which has been mentioned by others [16,17]. At a radial location around $r/D = 1$, a counter-rotating vortex, i.e. the secondary vortex, was possibly generated at the ground due to wall friction. The primary and secondary vortices could narrow down the flow path and stretch the flow between them, causing a locally accelerated flow, and also add a positive w velocity component by lifting up the local flow. Also affected by this vortex pairs, the trend of tangential velocity v at $r/D = 1$ was more complicated than other radial locations where tangential velocities were almost zero.

Fig. 9 shows the overall and the three turbulence intensity components at different radial locations, calculated by normalizing the root-mean-square (RMS) of the velocity fluctuation by the local mean of the resultant velocity ($U = \sqrt{u^2 + v^2 + w^2}$). Generally, it

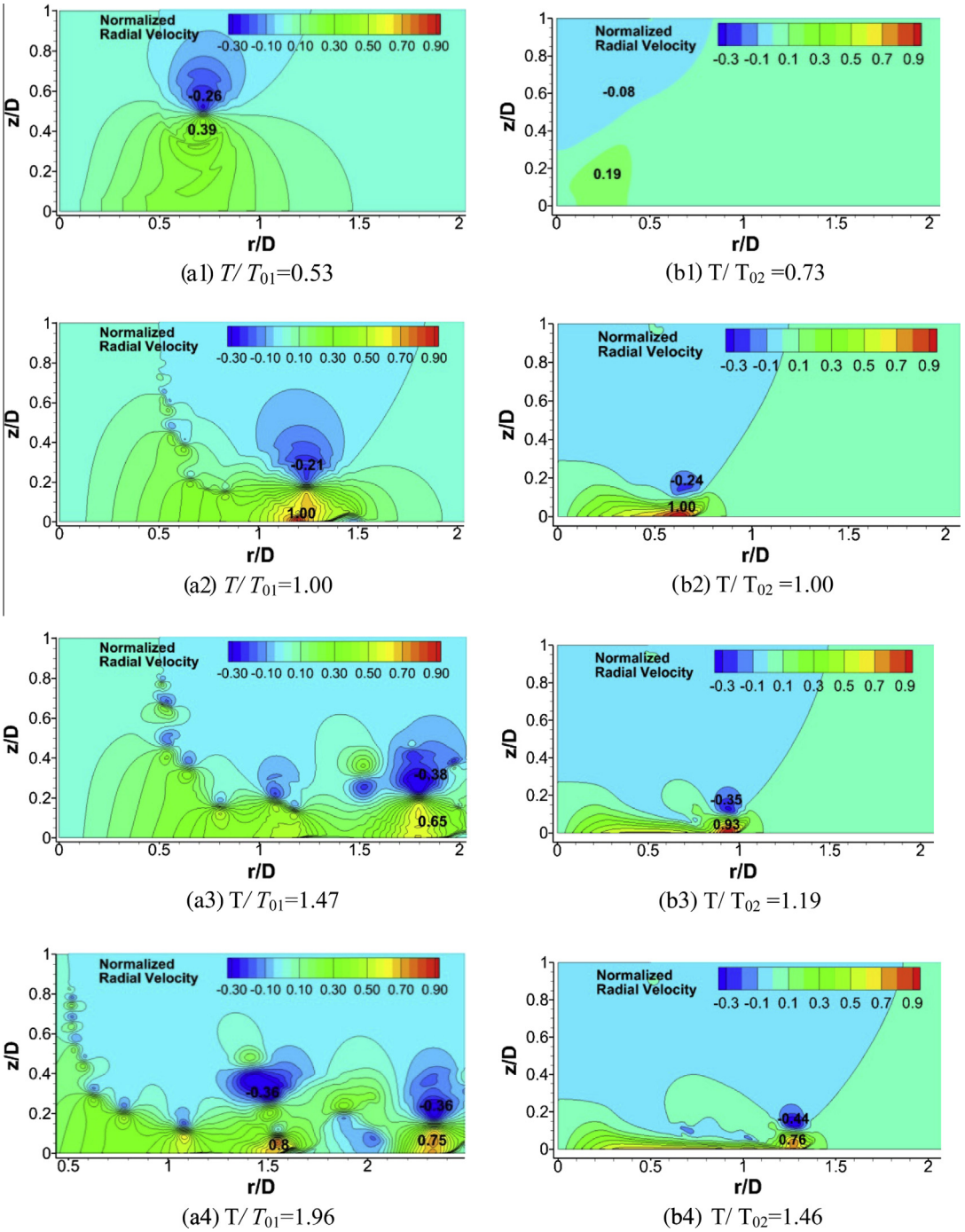

Fig. 14. Contour of normalized radial velocity (Numerical simulation) (a1–a4 impinging jet model; b1–b4 cooling source model).

is clear that the turbulence intensity decreased as the height increased from $z/D = 0$ to approximately $z/D = 0.05$ (where peak velocity occurred). However, it increased significantly above $z/D = 0.1$ and reached a constant value above $z/D = 0.25$ approximately. This turbulence profile is dramatically different from that of an atmospheric boundary layer, where turbulence intensity is larger near ground due to friction and disturbances. As the radial distance from the center increased, turbulence intensity near ground increased notably and the slope of the curve became milder, indicating enhanced flow mixing and reduced wind speed. Furthermore, the w-component turbulence intensity behaved differently from that of other components. Fluctuation of the vertical component was found significantly lower than those of other components at locations very near the ground due to the wall effects. However, with the height increased, fluctuation of w component increased dramatically and contributed the largest at $r/D = 1.0$ and $r/D = 1.5$. Nevertheless, for $r/D = 2$ and larger, the peak value of the w component turbulence intensity dropped and eventually followed the same trends of other components. The significant fluctuation in vertical direction might be closely related to the shedding vortices within the shear layer, which will be further discussed later.

4.1.2. Whole-field flow characteristics

The ensemble-averaged PIV results for H/D = 1 case are presented in Fig. 10, which shows distributions of velocity and turbulence in the wall-jet region. It can be seen that the jet flow expanded as it approached the ground. As shown in Fig. 10a, radial velocity u was almost zero at the center of the stagnation region. As the flow diverged away from the core center, it accelerated at first,

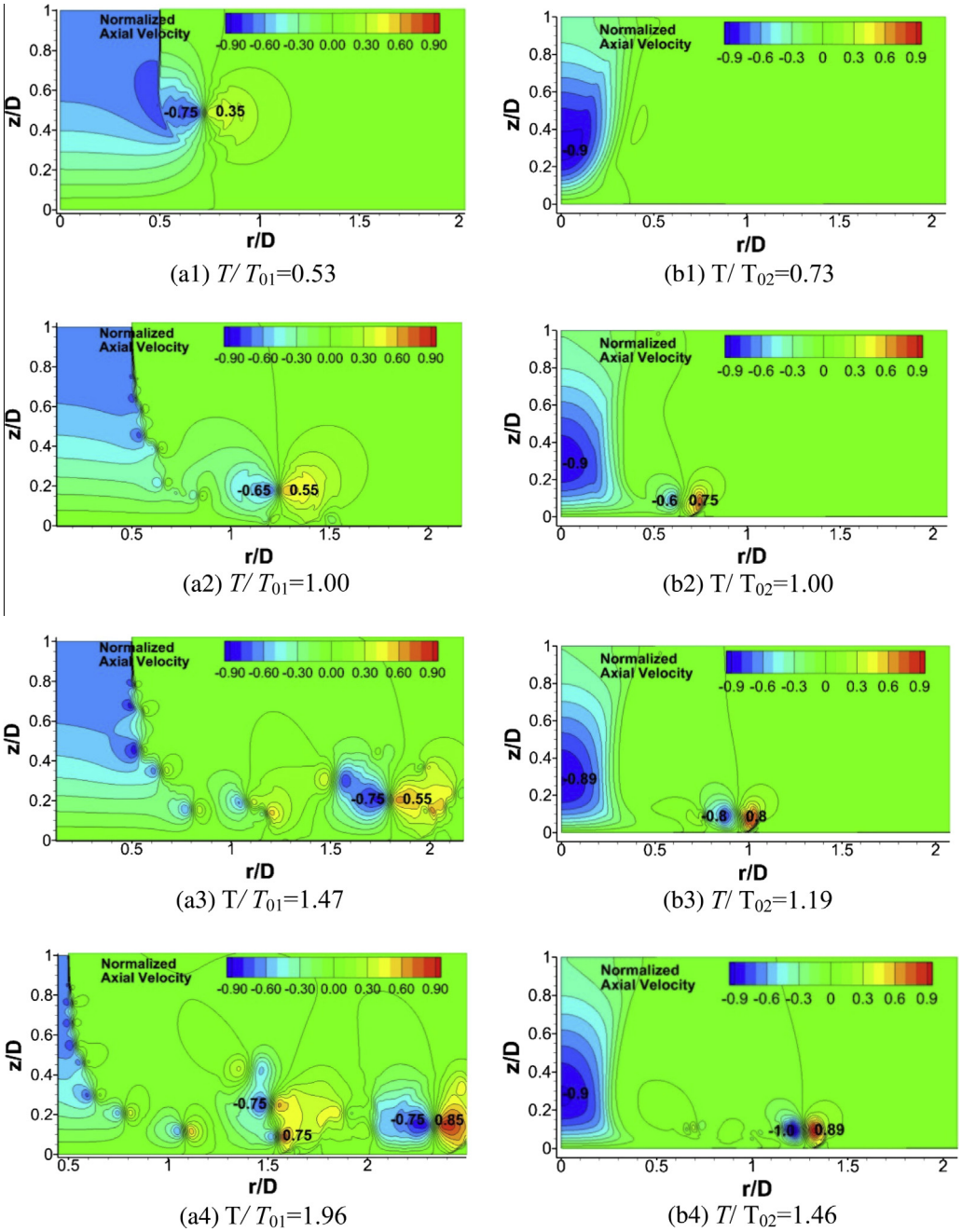

Fig. 15. Contour of normalized axial velocity (Numerical simulation) (a1–a4 impinging jet model; b1–b4 cooling source model.

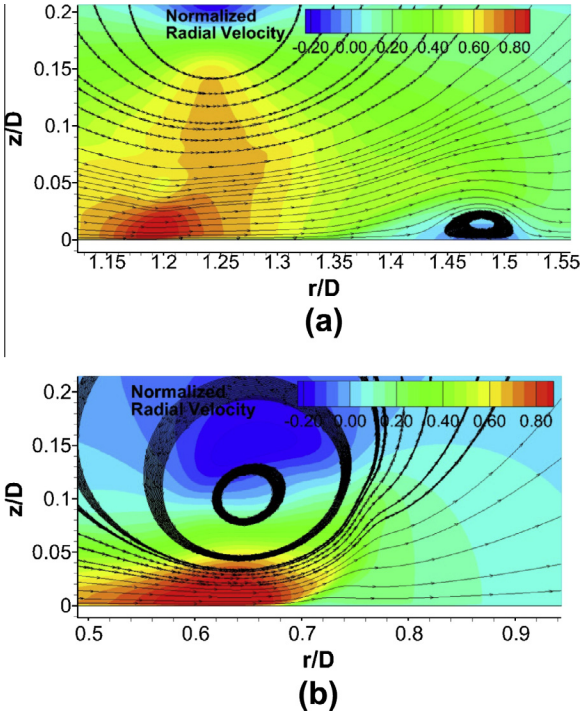

Fig. 16. Streamlines at the $T/T_{01} = 1.00$ and $T/T_{02} = 1.00$ (Numerical simulation) (a) impinging jet model, (b) cooling source model.

reached its maximum speed at the location of $r/D \approx 1.0$, and then slowed down gradually further downstream. A high velocity region with a maximum magnitude of more than $u/V_{jet} = 1.1$ ($V_{jet} \approx 6.9$ m/s) covered a considerable area from $r/D = 0.7$ to $r/D = 1.0$. The depth of outflow expanded as flow travelled radially, illustrated by the shape of the contour. In Fig. 10b, a region of accelerated flow is seen where w changes to positive values from negative values (downward direction) in the downdraft region.

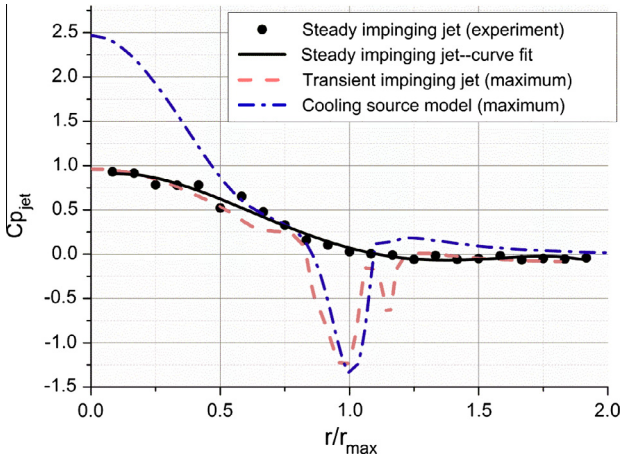

Fig. 18. Comparison of pressure distribution along radial direction (Experiment: steady impinging jet; numerical: transient impinging jet/cooling source).

Fig. 10c and Fig. 10d show the turbulence kinetic energy and Reynolds shear stress, which were normalized by the squared jet velocity (V_{jet}^2). It can be seen clearly that the turbulence level within the core region of the steady impinging jet (i.e., $r/D \leqslant 0.5$) is quite low. The turbulence intensity was found to increase greatly in the outflow region of the steady impinging jet (i.e., $r/D > 1.0$). A region with very high turbulence intensity (i.e., much higher turbulence kinetic energy) was found to exist at the downstream location of $r/D \approx 1.5$–2.0. Generally, the turbulence was generated from two sources: the interface between the jet flow and the boundary layer on the ground. Turbulent flow arising from these two sources then mixed to form a large turbulence region in the wall jet flow. In the Reynolds-shear–stress contour, turbulence from these two sources can be easily distinguished. The negative regions were caused by a negative velocity gradient in the vertical direction and therefore represented the turbulent flow formed at the

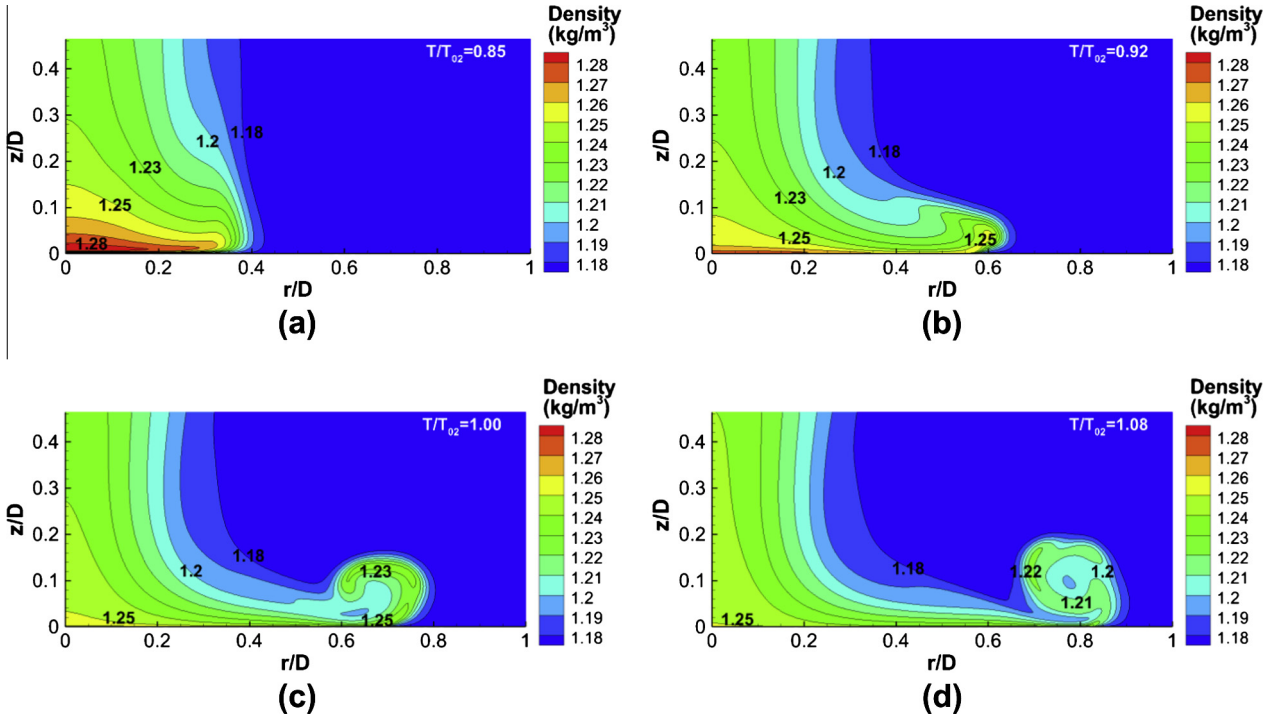

Fig. 17. Density contours at different time steps (Numerical simulation) $T/T_{02} = 0.85$, (b) $T/T_{02} = 0.92$, (c) $T/T_{02} = 1.00$, (d) $T/T_{02} = 1.08$.

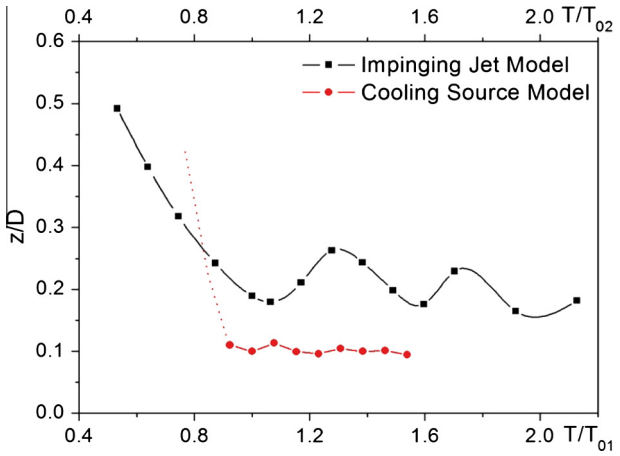

Fig. 19. Trajectories of the primary vortex cores of two models in axial direction (Numerical simulation).

interface due to the strong shear. In contrast, the red region showed the turbulence developed in the wall-jet boundary layer.

4.1.3. Time-domain characteristics of the steady impinging jet

In the previous section, ensemble-averaged information of the microburst outflow was shown in detail. Turbulence mixing was remarkable in the shear layer due to flow instability. However, it was found that turbulence in shear layer actually contains large-scale movement of the periodically-shed vortices. Fig. 11 shows Fast Fourier Transformations of the velocity time history at a height of $z/D = 0.2$, which could be considered within the shear layer of the wall-jet flow. It can be seen in Fig. 11a that, instead of complete randomness, a low-frequency component near $f \approx 16$ Hz dominated the spectrum at $r/D = 1$, corresponding to a Strouhal number $St = 1.63$ ($St = fD/V_{jet}$). This number is very close to that obtained in O'Donovan and Murray [34]. As the flow moved to $r/D = 2$ (Fig. 11b), the dominant frequency and its magnitude decreased as the flow velocity decreased and the large-scale structure broke down into many smaller ones. This phenomenon was further verified in Fig. 12, which presents a single snapshot of the instantaneous flow in the investigated window 2B. Vorticity was calculated as $\frac{\partial w}{\partial x} - \frac{\partial u}{\partial z}$. In this figure, two primary vortices could be clearly visualized at the flow interface. Therefore, if the generation and expansion of the primary vortex is assumed to be the major characteristic of a natural microburst event, the steady impinging jet flow could be seen as a combination or an ensemble-average of a series of microburst events with sufficiently long period.

In Fig. 13, the averaged velocity profiles at the maximum velocity locations were extracted and compared with the field data and the previous numerical and experimental results. In this plot, the vertical distance 'z' was non-dimensionalized by 'b', which denotes the height where the radial wind speed (u) is half of its maximum (u_{max}) and radial velocity u is normalized by u_{max}. It can be seen in the plots that there is very good agreement between these measurements and the field data, particularly for $H/D = 2$. It should also be noted that considerable discrepancies was present between the point-measurement results and the PIV results over $z/b = 1.0$. These discrepancies may arise from the measurement error of the cobra-probe, whose accuracy was dramatically decreased in the shear layer where flow direction rapidly changes.

Therefore, even though the time-dependent information is neglected in the steady impinging jet model, the similarity of the velocity profiles suggests that it could still be used as a valid simulation model for quasi-steady study.

4.2. Numerical simulation: comparison of transient characteristics of the impinging jet model and the cooling source model

4.2.1. Comparison of velocity and surface pressure distribution

To obtain an intuitive sense of the differences in the transient features of impinging jet model and cooling source model, the evolution of velocity fields of the two models was first analyzed and compared. Velocity was normalized by the maximum wind speed obtained during each simulation, namely V_{01} and V_{02}. Fig. 14 shows the contours of normalized radial velocity component for two modeling methods at different scaled time. The four contours were organized by matching the locations of the first vortex core, i.e. before touching the ground, at r_{max}/D, $1.5r_{max}/D$, and $2r_{max}/D$, where r_{max} is the radial location where the maximum radial velocity occurred. As shown in Fig. 14(a1), the impinging jet produced a pair of negative and positive velocity contours, i.e., a primary vortex, before the flow touched the ground. As the primary vortex touched the ground at $T/T_{01} = 1.00$, the outflow was stretched and accelerated within the channel between the primary vortex and the secondary vortex as caused by ground friction. These vortices can be clearly seen in Fig. 16. The spatial and temporal maximum velocity of each model was found at this time to accompany the primary vortex. As the vortex traveled and decayed radially, new vortices were found to continuously form at the shear layer between the jet flow and the ambient air. These subsequently-formed vortices then produced a series of large-velocity regions that were comparable with the maximum velocity, as shown in Fig. 14(a3 and a4).

The radial–velocity contours of the cooling source model exhibited significant differences from those of the impinging jet model. In contrast to the case of impinging jet model, no significant reverse flow occurred at the jet-ambient interface before the flow touched the ground as shown in Fig. 14(b1). Maximum velocity was found at $T/T_{02} = 1.00$ accompanied with the traveling primary vortex as shown in Fig. 14(b2). Due to a different forcing parameter and gravitational effects, the velocity contour was apparently more compressed near the ground than that of the impinging jet model. As the outflow traveled radially, the reverse-flow velocity inside the primary vortex was found to be more significant than that of the impinging jet model. Most importantly, no follow-up vortices developed after the primary vortex. The primary vortex accompanied with the large velocity region decayed with time and eventually died out after the strength of the cooling source decreased to zero. As shown in Fig. 16, no secondary vortex was found at the time when maximum velocity occurred.

The normalized axial velocity contours produced by the two modeling are presented in Fig. 15, with a same time sequence as Fig. 14. It can be seen that the axial velocity distributions in the downdraft core of the two models were different. For the impinging jet model, the flow exhausted from the jet exit remained constant until it started to decelerate towards the ground at a height of $z/D = 0.6$. However, for the cooling source model, flow accelerated due to gravity and reached maximum at a height of $z/D = 0.3$ before it slowed down towards the stagnation point. As the flow expanded radially, it can be seen that the axial velocity component induced by the primary vortex was significant in both two cases. Particularly in the cooling source model, the maximum axial velocity was found to have same magnitude with the maximum radial velocity. This considerable axial velocity component is crucial for the safety of aircrafts and civil structures. However, this time-dependent phenomenon apparently cannot be studied using steady impinging jet model and usually is hard to be detected by a Doppler radar in the field.

Generally, differences in velocity fields depicted above mostly resulted from the formation and transportation of the primary vortex. As discussed earlier, the primary vortex in the impinging jet model formed at early downdraft stage due to strong shear at

the interface. However, the formation of the primary vortex in the cooling source model was a completely different process. Fig. 17 shows the density map of the cooling source model at different time steps. It can be seen clearly that the leading edge of the denser air gradually rolled up as it traveled in radial direction. Therefore instead of being transported from the upstream in the impinging jet model, the primary vortex in the cooling source model actually generated locally at the leading edge of the outflow and resembled the features of a gravity current head [35].

Differences of underlying physics can be also seen from the surface pressure distributions in Fig. 18, where pressure coefficients of transient impinging jet (at $T/T_{01} = 1$), cooling source model (at $T/T_{02} = 1$) and the experimental steady impinging jet were compared. Pressure coefficient is defined as $Cp_{jet} = (P - P_{atm})/0.5\rho V_{jet}^2$ for both transient and steady impinging jet, where ρ is constant and V_{jet} is constant jet velocity. For cooling source model, maximum ρ and V_{jet} at $T/T_{02} = 1$ were chosen to be the maximum along the central axial axis from varying density and velocity distributions. A good match between the results of transient and steady impinging jet was found except that a large negative pressure was found at $r/r_{max} = 1$ for the transient impinging jet model. Due to the existence of secondary vortex in the transient impinging jet, a smaller peak of negative pressure could also be seen at this time step. Similar minimum pressure was found for both transient impinging jet and cooling source models corresponding to the location of the primary vortex of the two models. However, a large deviation was seen at the center of the flow field. For both transient and steady impinging jet, Cp_{jet} is equal to 1 at the center due to the stagnation of jet flow, whereas a much larger Cp_{jet} was found at the center for the cooling source model due to the contribution of the hydrostatic pressure of the denser air. Therefore, a much higher pressure load would be expected when a civil-structure model was located within the core region, if the microburst is simulated using cooling source model. However, the transient loading effects outside the core region caused by the primary vortex could be similar for these two modeling methods.

4.2.2. Comparison of the primary vortex trajectory

Based on discussion in previous sections, the most dominant feature of the transient microburst flow is the primary vortex. Besides the formation of the primary vortex, it is also of great importance to understand how primary vortices move in the expanding outflow for transient impinging jet and cooling source models.

Fig. 19 shows the height of the primary vortex core as a function of time for two models. The vortex core was located by tracking the lowest pressure point within the primary vortex. Because of strong instability at the interface of the wall-jet flow, the primary vortex descending from a high-altitude position in the impinging jet model was found to oscillate in the vertical direction as it expanded radially. However, the primary vortex in the cooling source model appeared rather stable as it moved outwards. Because of gravity, the vortex was also found to be much closer to the ground.

The radial-direction trajectories of the primary vortex cores were compared with field data gathered from the JAWS project [5] in Fig. 20. To make this comparison valid, the field data in this study was re-normalized to ensure that $r/r_{max} = 1$ corresponds to the normalized time $T/T_0 = 1$, where T_0 represents T_{01} for the impinging jet model and T_{02} for the cooling source model, respectively. It should be noted that the field data does not represent the actual vortex core movement, but rather the expansion of the gust front of the microburst. Hence, it is assumed here that the vortex expansion is equivalent to or similar to the gust front expansion. From this figure, it is clear that both the impinging jet model and the cooling source model resulted in a linearly-expanded primary vortex, similar to real microburst events in nature. The slope of each curve represents the relative expansion speeds corresponding to the initial conditions of each of the real or simulated microburst events, which could be different from case to case.

4.2.3. Comparisons with the field data

Based on the previous discussions, the differences between the two models were significant and considerable simplifications were made in both two modeling methods. To better serve the research purpose, a comparison with field data is necessary to evaluate the validity of different modeling methods.

In Fig. 21, time series of the radial velocity profiles were compared with the time history of a single microburst event occurring during the JAWS project [5]. In this typical microburst event, the maximum velocity increased dramatically and reached its peak at time 16:48. The maximum velocity location moved away from the center as the primary vortex expanded. This time-series data covered 9 min of the entire event. However, matching the simulation results and the field data in time dimension is difficult due to the random nature of the microburst event. This comparison was made by matching the maximum velocity at $T/T_0 = 1$ of two modeling results. Velocity was normalized by the maximum velocity at $T/T_0 = 1$ and radial distance was normalized by r_{max}, which is defined as the radial distance where maximum radial velocity occurred that is different in the field and experiment. It can be seen that both models provided reasonably good estimations of dynamic features of the outflow expansion within the range of the maximum velocity location. Nevertheless, the prediction is poor beyond the maximum velocity location, probably due to the complexity of the atmospheric conditions in a real microburst event.

A transient microburst event is actually a four dimensional problem, which does not only evolves in space but also changes rapidly in time domain. From an engineering point of view, the most interesting part is to examine the maximum wind which could be induced by the microburst and the velocity distribution at the maximum wind condition. However, it should be admitted that the wind profiles at the maximum condition is highly dependent on when and where the data was extracted particularly in a transient simulation. Therefore in order to eliminate the uncertainty, data was extracted from the spatial and temporal vicinity of the computed maximum wind condition and compared with the field data and the results of previous studies in Fig. 22. The field data are usually collected by Doppler radar within a very short time period and a certain spatial range. Hence, from whole-event point of view, the field data could still be seen as a snapshot of the entire microburst event. Fig. 22a shows the radial velocity profiles at the maximum velocity time and in the vicinity of the maximum velocity location for both models. It is evident that the transient impinging jet data deviated considerably from both the steady impinging jet data and the field data, while the cooling source resulted in an instantaneous velocity profile similar to that of the field data up to the boundary-layer height (b). This result was further verified by comparing with the data of the previous studies. Vermeire et al. [31] obtained a similar velocity profile using the impinging jet model which had a large discrepancy compared with the field data, while the profile generated by cooling source function showed a good match. Mason [33] also generated a maximum-storm velocity profile following the trend of the field data. Slight deviation under $z/b = 1$ is possibly due to the secondary vortex reported in his research caused by the surface roughness, which were not considered in this study. Similar results could be found in Fig. 22b, in which the velocity profiles were compared by taking data from the vicinity of the maximum velocity time.

These results imply that because of the similar trajectories of the primary vortex in radial direction, transient impinging jet and cooling source models were both valid in terms of predicting the time-dependent velocity distribution along radial direction. However, due to the intrinsic differences of the formation and

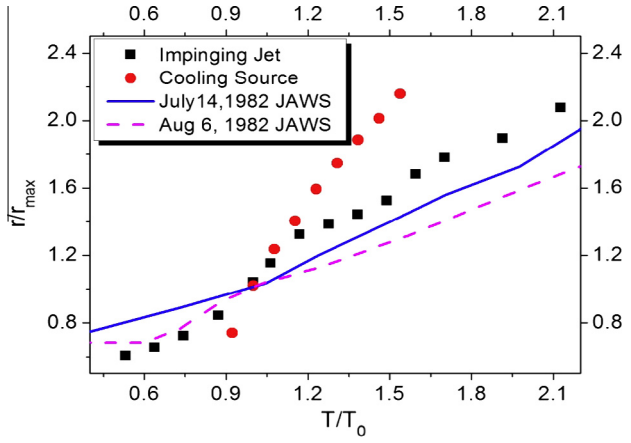

Fig. 20. Trajectories of the primary vortex cores of two models in radial direction (Numerical simulation, T_0 given in Table 1, JAWS data provided by Hjelmfelt [5]).

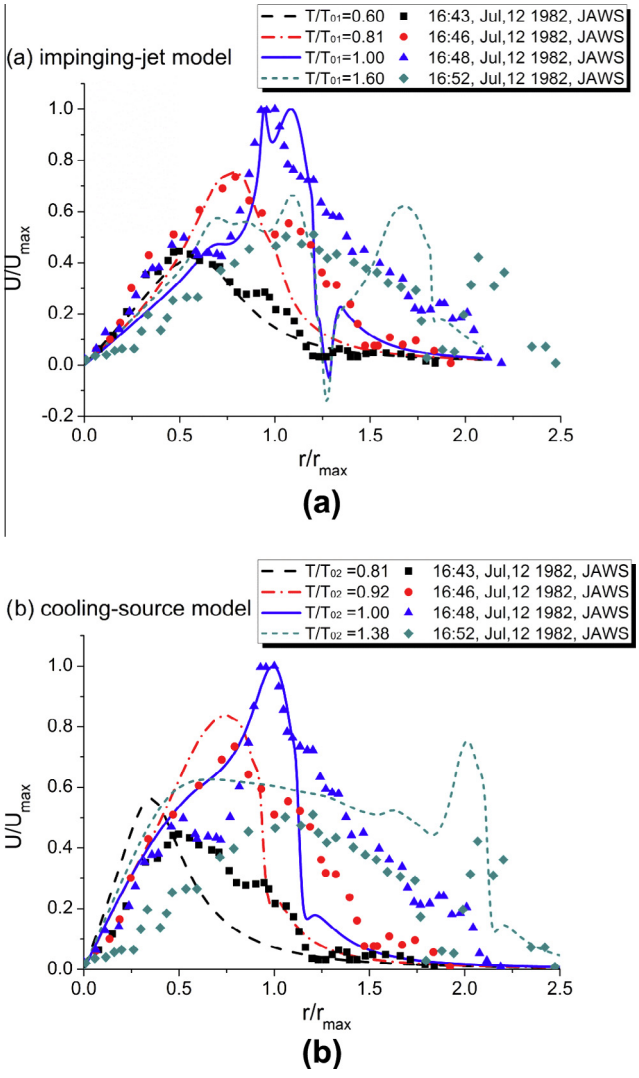

Fig. 21. Comparison of the time series of velocity profiles in radial direction (a) impinging jet model, (b) cooling source model (Numerical simulation; JAWS data provided by Hjelmfelt [5]).

structure of the primary vortices, the maximum velocity profiles at the critical location of two models were dramatically different. Apparently, the "rolling-up" type primary vortex generated in a

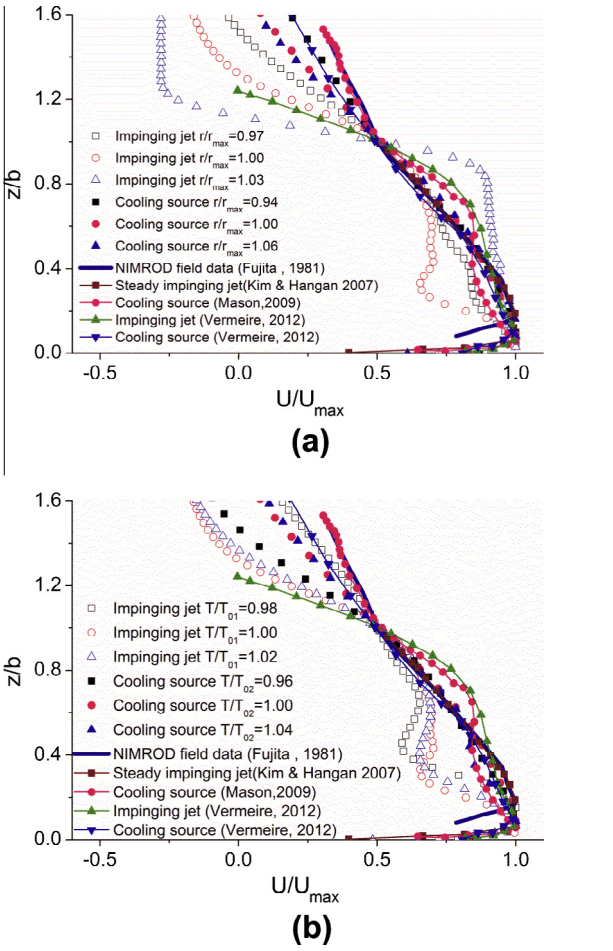

Fig. 22. Comparison of radial velocity profiles: (a) at the vicinity of the maximum velocity location at the time of its occurrence, (b) at the vicinity of the maximum velocity time (Numerical simulation).

cooling source model is more similar to the field event than that of an impinging jet model.

5. Concluding remarks

In the present study, the microburst outflow was first simulated experimentally using steady impinging jet model. Both point measurements and whole-field measurements (PIV) were conducted to study the flow field. Results showed a detailed picture of overall/componential velocity and turbulence within a steady impinging jet flow. Comparisons suggested that the wind profile at the critical location matched well with the field data and the previous research. FFT of the velocity time-history and instantaneous PIV results implied the turbulence in the shear layer was dominated by shedding vortices at a low frequency ($St = fD/V_{jet} = 1.63$). Therefore, it was suggested that the steady impinging jet model could be seen as a statistical average of a series of simulated microburst events.

Numerical simulations were performed to compare different transient outflow characteristics between the transient impinging jet model and the cooling source model. The comparisons of velocity contours and vortex trajectories between the impinging jet model and the cooling source model revealed several different characteristics induced by intrinsically different underlying physics. While the flow patterns in the impinging jet model were dominated by instability in the shear layer, the cooling source model

produced a relatively smooth outflow resembling the features of gravity current. Due to the strong shear at the interface, a primary vortex was found to form immediately after the flow was initiated in the transient impinging jet model. As the primary vortex touched the ground and expanded radially, follow-up vortices were continuously generated and produced a series of large-velocity regions that were comparable with the maximum velocity. However, for the cooling source model, the primary vortex was found to be formed only after the cooled air descended to the ground. Denser air was found to roll up to form the primary vortex at the leading edge of the outflow. No follow-up vortices like those of the impinging jet model were found.

Surface pressure distributions were also investigated. While the negative pressures induced by the primary vortices was similar between the two models, the cooling source model produced much higher pressure in the core region due to the extra contribution from the hydrostatic pressure. A secondary peak of negative pressure was found in the transient impinging jet corresponding to the secondary vortex found at the maximum-velocity time.

The trajectories of the primary vortex in these two models show distinct features. In impinging jet model, the primary vortex propagated in a wavy fashion whereas in the cooling source model it remained at a rather constant height. The transient expansion of the primary vortex in these two models, though exhibiting different speeds, resembles the linear characteristic of the natural events.

Comparisons were performed between transient velocity profiles of each of the two modeling methods and the field data. Results indicated that, transient impinging jet and cooling source models were both valid in terms of predicting the time-dependent velocity distribution along radial direction. However, in terms of reproducing the instantaneous radial–velocity profile at the maximum wind condition, the impinging jet model deviated from the field data, while the cooling source model provided more reasonable agreement.

The merits and demerits of each modeling method are summarized as follows:

(1) The steady impinging jet model provided an averaged flow field with a reasonable radial–velocity profile at the critical location (maximum velocity location), but it lacks time-dependent information. It is simple to simulate and convenient for quasi-steady wind load test on laboratory models.
(2) The transient impinging jet model provided a good simulation of the dynamic properties of the primary vortex expansion, but it failed to provide the instantaneous radial velocity profile resembling the field data at the critical location. Like the steady case, it is relatively easy to simulate in a laboratory with a reasonable scale.
(3) The cooling source model provided a good simulation of the instantaneous radial velocity profile similar to the field data at the critical location, and also gave a reasonable representation of the transient expansion of the primary vortex. Although successfully simulated numerically, the cooling source model is difficult to simulate in the laboratory environment, particularly with a sufficient scale to conduct wind load tests on scaled laboratory models.

In conclusion, since field data is rather scarce, the truth regarding real microbursts in nature is far from being fully-understood. Therefore, from an engineering point of view, the choice between the uses of the three microburst modeling methods should depend on the purpose. Future studies related to microburst modeling should attempt to take advantage of certain aspects of simplicity and accuracy while avoiding the drawbacks of each modeling method.

Acknowledgments

This study is funded by the US National Science Foundation (NSF) under Award No. CMMI-1000198. The authors would like to thank NSF for the financial support and acknowledge the help of Bill Rickard, department technician, and Nick Krauel, undergraduate student, at Iowa State University in building test models and experimental setups.

References

[1] Fujita TT. The downburst: microburst and macroburst. University of Chicago Press; 1985.
[2] Fujita TT. Spearhead echo and downburst near the approach end of John F. Kennedy runway. New York City: SMRP Res. Pap.; 1976.
[3] Wilson JW, Roberts RD, Kenssiger C, McCarthy J. Microburst wind structure and evaluation of Doppler radar for airport wind shear detection. J Climate Appl Meteor 1984;23:898–915.
[4] Hjelmfelt MR. The microbursts of 22 June 1982 in JAWS. J Atmos Sci 1987;44(12):1646–65.
[5] Hjelmfelt MR. Structure and life cycle of microburst outflows observed in Colorado. J Appl Meteorol 1988;27(8):900–27.
[6] Ivan M. A ring-vortex downburst model for flight simulations. J Aircraft 1986;23(3):232–6.
[7] Schultz T. Multiple vortex ring model of the DFW microburst. J Aircraft 1990;27:163–8.
[8] Vicroy D. Assessment of microburst models for downdraft estimation. J Aircraft 1992;29(6):1043–8.
[9] Selvam RP, Holmes JD. Numerical simulation of thunderstorm downdrafts. J Wind Eng Ind Aerodyn 1992;44(1–3):2817–25.
[10] Holmes JD. Modelling of extreme thunderstorm winds for wind loading of structures and risk assessment. In: Larson A, Larose GL, Livesey FM, editors. Wind engineering into the 21st century. Balkema: Rotterdam; 1999. p. 1409–15.
[11] Letchford CW, Illidge G. Turbulence and topographic effects in simulated thunderstorm downdrafts by wind tunnel jet. In: Larson A, Larose GL, Livesey FM, editors. Wind engineering into the 21st century. Balkema: Rotterdam; 1999. p. 1907–12.
[12] Holmes JD, Oliver SE. An empirical model of a downburst. Eng Struct 2000;22:1167–72.
[13] Wood GS, Kwok CS, Motteram NA, Fletcher DF. Physical and numerical modelling of thunderstorm downbursts. J Wind Eng Ind Aerodyn 2001;89:535–52.
[14] Choi ECC. Field measurement and experimental study of wind speed profile during thunderstorms. J Wind Eng Ind Aerodyn 2004;92:275–90.
[15] Chay MT, Albermani F, Wilson R. Numerical and analytical simulation of downburst wind loads. Eng Struct 2005;28:240–54.
[16] Kim J, Hangan H. Numerical simulation of impinging jets with application to downbursts. J Wind Eng Ind Aerodyn 2007;95:279–98.
[17] Das KK, Ghosh AK, Sinhamahapatra KP. Investigation of the axisymmetric microburst flow field. J Wind Eng 2010;7:1–15.
[18] Sengupta A, Sarkar PP. Experimental measurement and numerical simulation of an impinging jet with application to thunderstorm microburst winds. J Wind Eng Ind Aerodyn 2008;96:345–65.
[19] Mason MS, Letchford CW, James DL. Pulsed wall jet simulation of a stationary thunderstorm downburst. Part A: Physical structure and flow field characterization. J Wind Eng Ind Aerodyn 2005;93:557–80.
[20] Nicholls M, Pielke R, Meroney R. Large eddy simulation of microburst winds flowing around a building. J Wind Eng Ind Aerodyn 1993;46:229–37.
[21] Chay MT, Letchford CW. Pressure distributions on a cube in a simulated thunderstorm downburst. Part A: Stationary downburst observations. J Wind Eng Ind Aerodyn 2002;90:711–32.
[22] Letchford CW, Chay MT. Pressure distributions on a cube in a simulated thunderstorm downburst. Part B: Moving downburst observations. J Wind Eng Ind Aerodyn 2002;90:733–53.
[23] Sengupta A, Haan FL, Sarkar PP, Balaramudu V. Transient loads on buildings in microburst and tornado winds. J Wind Eng Ind Aerodyn 2008;96:2173–87.
[24] Lundgren TS, Yao J, Mansour NN. Microburst modeling and scaling. J Fluid Mech 1992;239:461–88.
[25] Yao J, Lundgren TS. Experimental investigation of microbursts. Exp Fluids 1996;21:17–25.
[26] Alahyari A, Longmire EK. Dynamics of experimentally simulated microbursts. AIAA J 1995;33(11):2128–36.
[27] Anderson JR, Orf LG, Straka JM. A 3-D model system for simulating thunderstorm microburst outflows. Meteorol Atmos Phys 1992;49:125–31.
[28] Orf LG, Anderson JR, Straka JM. A three dimensional numerical analysis of colliding microburst outflow dynamics. J Atmos Sci 1996;53(17):2490–511.
[29] Orf LG, Anderson JR. A numerical study of traveling microbursts. Mon Weather Rev 1999;127:1244–58.
[30] Mason MS, Wood GS, Fletcher DF. Numerical investigation of the influence of topography on simulated downburst wind fields. J Wind Eng Ind Aerodyn 2010;98:21–33.

[31] Vermeire BC, Orf LG, Savory E. Improved modelling of downburst outflows for wind engineering applications using a cooling source approach. J Wind Eng Ind Aerodyn 2011;99(8):801–14.
[32] Launder BE, Spalding DB. The numerical computation of turbulent flows. Comput Methods Appl Mech Eng 1974;3:269–89.
[33] Mason MS, Wood GS, Fletcher DF. Numerical simulation of downburst winds. J Wind Eng Ind Aerodyn 2009;97:523–39.
[34] O'Donovan TS, Murray DB. Jet impingement heat transfer – Part II: A temporal investigation of heat transfer and velocity distributions. Int J Heat Mass Transfer 2007;50:3302–14.
[35] Benjamin TB. Gravity currents and related phenomena. J Fluid Mech 1968;31(2):209–48.